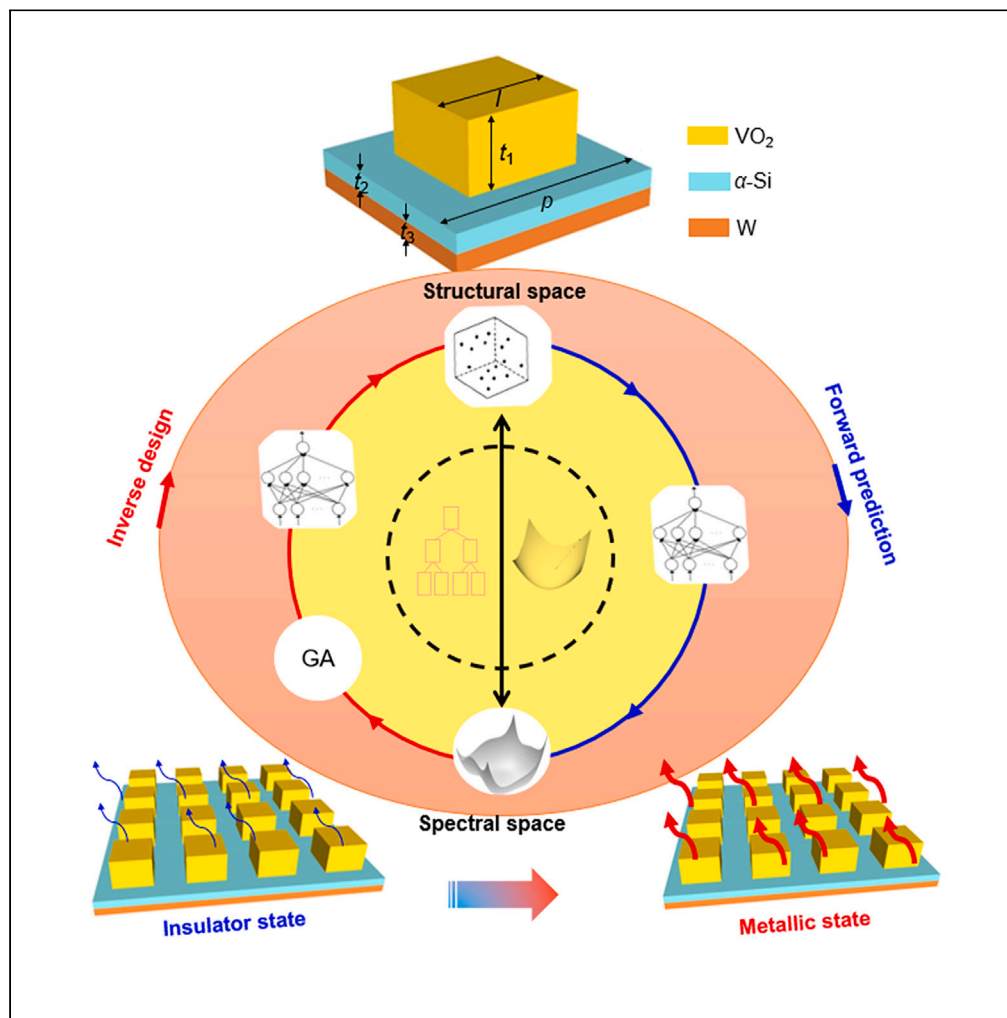**Article**

Machine learning enabled rational design for dynamic thermal emitters with phase change materials

Jining Wang,
Yaohui Zhan, Wei
Ma, Hongyu Zhu,
Yao Li, Xiaofeng Li

yhzhan@suda.edu.cn (Y.Z.)
xfli@suda.edu.cn (X.L.)

Highlights

Accurate neural network (NN) models have been trained for dynamic thermal emitters

Superior emittance tunability has been achieved with simple configurations

NN-aided genetic algorithm makes the inverse design with extreme performance feasible

Article

Machine learning enabled rational design for dynamic thermal emitters with phase change materials

Jining Wang,[1] Yaohui Zhan,[1,*] Wei Ma,[2] Hongyu Zhu,[1] Yao Li,[3] and Xiaofeng Li[1,4,*]

SUMMARY

Dynamic thermal emitters have attracted considerable attention due to their potential in widespread applications such as radiative cooling, thermal switching, and adaptive camouflage. However, the state-of-art performances of dynamic emitters are still far below expectations. Here, customized to the special and stringent requirement of dynamic emitters, a neural network model is developed to effectively bridge the structural and spectral spaces and further realizes the inverse design with coupling to genetic algorithms, which considers the broadband spectral responses in different phase-states and utilizes comprehensive measures to ensure the modeling accuracy and computational speed. Besides achieving an outstanding emittance tunability of 0.8, the physics and empirical rules have also been mined qualitatively through decision trees and gradient analyses. The study demonstrates the feasibility of using machine learning to obtain the near-perfect performance of dynamic emitters, as well as guiding the design of other thermal and photonic nanostructures with multifunctions.

INTRODUCTION

Dynamic thermal emission control has attracted considerable attention in the fields of radiative cooling,[1–4] adaptive camouflage,[5–9] thermostats,[10,11] thermochromic smart windows,[12–14] spacecraft thermal control[15,16] and thermophotovoltaic cells.[17–19] Among various dynamic thermal emission devices, the VO$_2$-based dynamic emitter is a promising representative, which undergoes a reversible metal-to-insulator transition (MIT) at a critical temperature T_c (68°C for intrinsic VO$_2$).[20,21] The occurrence of MIT is always accompanied by a dramatic change in the optical properties, which transforms the phase-change material from an infrared lossless "insulator state" ($T<T_c$) to an infrared lossy "metallic state" ($T>T_c$).[22] To exploit this intriguing property, many VO$_2$-based emitters are investigated theoretically and experimentally for intelligent thermal modulation. Taylor et al. proposed an asymmetric Fabry-Perot emitter, which consists of a sandwiched configuration with a lossless dielectric spacer inserted between a VO$_2$ thin film and an opaque metal substrate, and displayed a total emittance change of over 0.45 across the VO$_2$ phase transition.[23,24] Omam et al. designed an Al/VO$_2$/Dolomite multilayered film to generate hybrid Fano resonances, realizing a temperature-dependent near-unity narrowband emission, which might be a promising alternative for the temperature or biochemical sensors.[25] Hu et al. demonstrated a spatiotemporal modulation platform based on thermal hysteresis emission characteristics of VO$_2$ phase-change materials, which achieved various thermotronic functionalities including negative-differential thermal emission, thermal diodes/transistors, and provided a unique perspective for dynamic thermal management.[26] Most recently, Wang et al. fabricated a kind of scalable smart windows composed of Low-E coating/Glass/Low-E coating/PMMA/VO$_2$ multilayers and presented distinct emissivities of 0.61 and 0.21 at high and low temperatures, manifesting excellent dynamic radiative cooling capability for self-adapting applications across different climate zones.[1] These planar multilayered devices, including those important but not enumerated,[27–29] have clear physical mechanisms and are scalable for mass production, laying a solid foundation for further performance enhancement.

Besides these planar configurations,[23–29] many artificial metamaterials with delicately designed nanostructures[30–34] have also been proposed, striving to push the boundaries of device performance and advanced functionality. For instance, Buhara et al. proposed a hybrid design by embedding the ultrathin VO$_2$ film into a silicon grating for thermal camouflage applications and numerically demonstrated the

[1]School of Optoelectronic Science and Engineering & Collaborative Innovation Center of Suzhou Nano Science and Technology, Key Lab of Advanced Optical Manufacturing Technologies of Jiangsu Province & Key Lab of Modern Optical Technologies of Education Ministry of China, Soochow University, Suzhou 215006, China

[2]State Key Laboratory of Modern Optical Instrumentation, College of Information Science and Electronic Engineering, Zhejiang University, Hangzhou 310027, China

[3]Center for Composite Materials and Structure, Harbin Institute of Technology, Harbin 150001, China

[4]Lead contact

*Correspondence:
yhzhan@suda.edu.cn (Y.Z.),
xfli@suda.edu.cn (X.L.)
https://doi.org/10.1016/j.isci.2023.106857

narrowband-to-broadband spectral tunability.[30] Long et al. fabricated a tunable VO_2 metasurface from an etch-free process and experimentally demonstrated a ∼6-fold enhancement of radiative thermal conductance on VO_2 phase transition.[31] Jia et al. designed a patterned VO_2 metamaterial arranged periodically on the multilayer substrate and a TiO2/polyethylene composite layer, obtaining an ultrahigh emissivity of 0.952 in the atmospheric window.[32] Zhang et al. devised a cooling system composed of a filter and a periodic trapezoidal VO_2-Ge multilayer absorber, the net cooling power of which theoretically meets the demanding requirement of dynamic radiative cooling in the daytime.[33] Lei et al. conceived a complex metamaterial composed of nested subcells, providing new freedom to manipulate the emission intensity and spectral bandwidth simultaneously.[34] Tang et al. proposed a mechanically flexible coating that consisted of an array of $W_xV_{1-x}O_2$ nanodisk embedded into the BaF_2 dielectric layer, realizing an emissivity tunability of 0.7 in the mid-infrared range (8–13 μm) and an absorption ratio of 0.25 in the solar spectral range (0.3–2.5 μm).[2] Although effective in dynamic switching, these designs either toward a narrowband emissivity undesired for radiative cooling or rely heavily on trial-and-error experiences lacking deep optimization to extreme performance and, in some cases, the invented metamaterials are too complex for cost-efficient production.

In this work, assisted by machine learning methods, we utilize a VO_2 metasurface with classic metal-insulator-metal architecture to investigate the possibility of realizing a simple configuration with near-perfect thermal modulation capability for radiative cooling. Instead of the conventional case-by-case method, we construct a purpose-designed machine learning architecture to automatically model and optimize three-dimensional dynamic emitters.[35–39] In the forward modeling process, the well-trained neural network functions as a fast prototyping tool with high accuracy comparable to full-wave simulations; whereas in the inverse design, the network is coupled with genetic algorithms to retrieve the optimized geometric parameters for the given spectral requirements. Although the machine learning approach has been widely applied to many fields,[18,19,40,41] its combination with the dynamic emitter has rarely been reported. By using an ensemble machine-learning toolkit, the implicit relationship between structural features and spectral responses is elucidated qualitatively. Different from the thermal switching at a specific wavelength, the concerned thermal emitter requires broadband emission tunability over the whole atmospheric window, which is highly desired for the emerging field of dynamic radiative cooling. The investigation designed successfully a dynamic emitter with a powerful machine-learning scheme, which also provides beneficial guidance for inversely designing other photonic and thermal devices.

RESULTS

Design purpose and strategy

The typical configuration of the dynamic emitter is shown in Figure 1A, which is composed of three layers from bottom to top including the metallic substrate (e.g., W layer), the dielectric spacer (e.g., Si layer), and the phase-change metasurface (e.g., VO_2 layer) that consists of an array of blocks ($l \times l \times t_1$) on a two-dimensional square lattice with a pitch of P. The thicknesses of the spacer and substrate are denoted as t_2 and t_3, respectively. The structural feature of the emitter can be described using the parametric vector of [P, l, t_1, t_2, t_3]. Owing to the nanoscale skin depth, the metallic substrate (or the substitute metallic film) is always thick enough to block the mid-infrared emission; therefore t_3 is set at a fixed value and then the variable structural vector is reduced to [P, l, t_1, t_2]. Besides the spatial dimension, the dynamic emitters have another degree of freedom to be considered, i.e., the two distinct working modes corresponding to the two phase-states of the VO_2 metasurface. As $T<T_c$, the VO_2-based emitter works in the insulator state and is expected to have low emittance to suppress the overcooling; as $T>T_c$, the emitter works in the metallic state and is desired to possess high emittance to enhance the radiative cooling. Therefore, the ideal requirement of the dynamic emitter for radiative cooling is maximizing the emittance at high temperatures, while minimizing the emittance at low temperatures across the whole atmospheric window.

For relieving the computational burden of three-dimensional full-wave simulations, as shown in Figure 1B, the neural network is built to relate the structural and spectral space of the system, which dramatically reduces the computational time and simultaneously ensures the modeling accuracy by utilizing the spectral decomposition, transfer learning methods and so on while taking account of the broadband spectral responses at both phase-states, making the genetic algorithm feasible for inversely optimizing the three-dimensional electromagnetic problems. The machine-learning toolkit such as the decision tree and gradient analysis is employed as an efficient way to enhance the model explanation. Figure 1C shows the mean square error (MSE) of the neural network prediction compared to numerical simulations, where 200 sets of structural parameters are sampled for both the metallic and insulator cases. As shown in
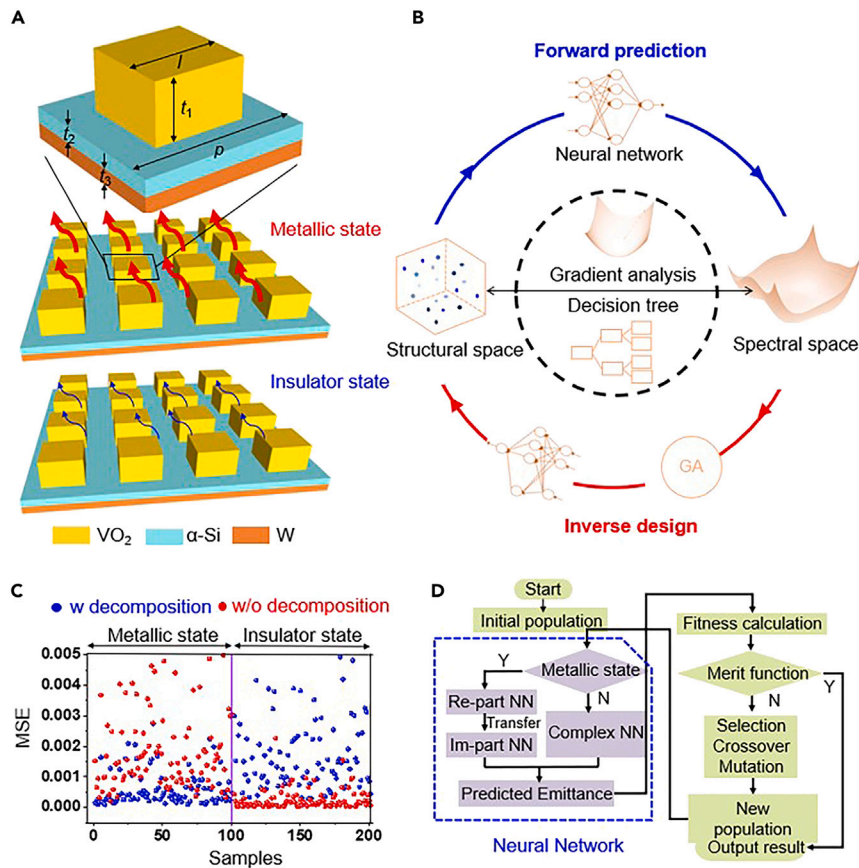
Figure 1. Schematic diagram of dynamic emitters and employed design strategies

(A) Dynamic emitter with phase-change metasurface. The dynamic emitter switches between the high-emissivity and low-emissivity modes as the VO_2 metasurface undergoes phase-changing from the metallic state to the insulator state, showing a fascinating tunability of emissivity in the mid-infrared regime.

(B) Synthetical approaches in this work to bridge the structural and spectral space of dynamic emitters. The neural network is utilized in not only the forward prediction (indicated by blue arrows) but also the inverse design (indicated by red arrows). The decision trees and gradient analysis are also employed to uncover the latent relations between the structural and spectral parameters.

(C) Loss evaluation of two training strategies: with (blue points) and without (red points) spectral decomposition. The samples with 200 sets of structural parameters, in both metallic and insulator states, are given for precision evaluation. The left-half panel distinguished by the purple line corresponds to the metallic state samples; whereas the right-half panel corresponds to the insulator state samples.

(D) Flowchart of the inverse-design process with a combination of the neural network (indicated by the dashed square and purple color) and the genetic algorithm (indicated by the green color). The initial structural configuration is randomly generated, the emittance of which is then predicted via different neural networks, determined by which phase condition is required. Next, the predicted emittance is imported into the genetic algorithm flow, such as the fitness calculation, merit function evaluation, and other routine operations.

Figure 1C, in the case of the metallic state, the neural network trained with the dataset of decomposed spectra (indicated by blue points) has much higher precision (average MSE $\approx 6.43 \times 10^{-4}$) than that of the undecomposed (MSE $\approx 2.75 \times 10^{-3}$); whereas in the case of the insulator state, the opposite is true – the neural network trained with the dataset of undecomposed spectra (indicated by red points) has much higher precision (MSE $\approx 2.60 \times 10^{-4}$) than that of the decomposed (MSE $\approx 2.48 \times 10^{-3}$). Accordingly, the neural networks for the real and imaginary parts of spectra are built respectively for the metallic state case. However, as shown in Figure 1D, the neural network for the imaginary spectra (Im-part NN) can be transferred from the neural network for the real part (Re-part NN) with aid of the transfer learning method, because of the inherent spectral similarity. It is noted that the transfer learning neural network might further increase the computational speed and accuracy. Furthermore, Figure 1D displays roughly
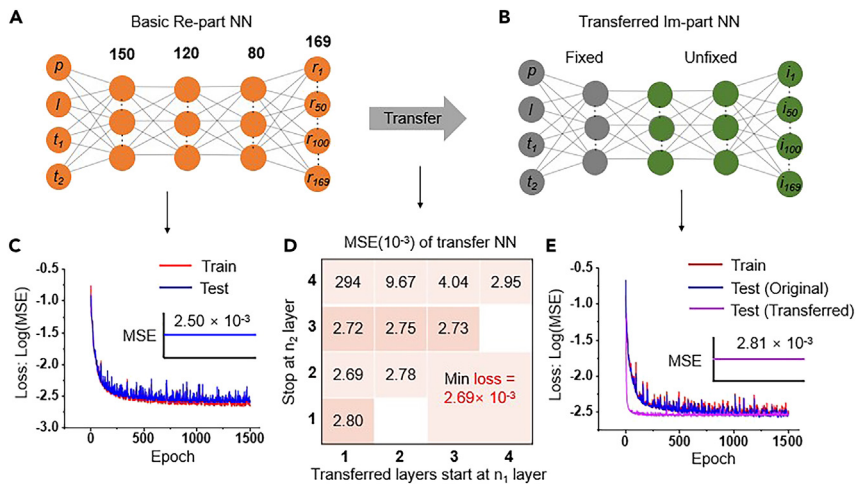
Figure 2. Transfer learning neural network for the real and imaginary spectra

(A) Neural network structure for the real-part emissivity spectra.

(B) Transferred neural network for the imaginary-part emissivity spectra.

(C) Loss values measured by logarithmic MSE during training and testing at different epochs, corresponding to the neural network in (A).

(D) Matrix table of the loss evaluation for the transferred neural network with the transferred layer starting at the n_1 layer and stopping at the n_2 layer.

(E) Loss values measured by logarithmic MSE during training and testing at different epochs, corresponding to the neural network in (B).

the flowchart of inverse design, which incorporates the neural network, as a substitute for the electromagnetic solver, in the global optimization process of the genetic algorithm.

The details of the transfer learning neural network are given in Figure 2. As shown in Figure 2A, the real part prediction network is constructed with the fully connected hidden layers of size {150, 120, 80}, where the same activation function of *tanh* is applied to match the data range of [-1, 1]. The output layer has 169 neurons corresponding to the same amount of spectral points. The action of the neural network can be expressed as a parameterized function *f*, which performs the following transformation,

$$spectrum = f(p, l, t_1, t_2; \theta)$$ (Equation 1)

The data-driven algorithm allows the neural network model to automatically infer and update the parameter θ from the training dataset to minimize the gap between the predicted and the label results.[42–44] However, as shown in Figure 2B, because Im-part NN and Re-part NN adopt the same network structure, θ of Im-part NN does not learn from the initial random value but updates from the transfer part of the well-trained Re-part NN that has a good prediction accuracy (as shown in Figure 2C). The matrix table in Figure 2D shows the averaged losses of the transferred neural networks with the transferred layer starting from the n_1 layer and stopping at the n_2 layer, where $1 \leq n_1 \leq 4$, and $n_1 \leq n_2 \leq 4$. As shown in Figure 2D, as the first two layers of Re-part NN are transferred, the best training effect of Im-part NN is obtained with a minimum loss of MSE = 2.69×10^{-3}. Besides the accuracy, as shown in Figure 2E, the epochs required for the transferred model to reach stability are reduced significantly compared to the direct training, which indicates the actual training time can be cut at least in half.

Spectral accuracy and model generality for forward prediction

To observe intuitively the performance of the neural network, we randomly select a few groups of structural parameters from the verification dataset and generate the spectral response via the trained neural network model, which is then compared with the full-wave simulations. Figure 3A shows the decomposed reflection coefficient (S_{11}) of the emitter with a parameter vector of [1.4, 1.1, 1.3, 0.2]. The spectra in Figure 3A correspond to the metallic state case, characterized by the dramatic variation across almost all of the spectral range. Despite so, the spectrum of Re(S_{11}) or Im(S_{11}) is more or less smoother than that of $|S_{11}|$, which might be the reason why the spectral decomposition has a positive impact on the prediction accuracy for the metallic case. As shown in Figure 3A, all the predicted spectra (dashed lines) of Re(S_{11}), Im(S_{11}), and $|S_{11}|$ coincide well with the full-wave simulations (solid lines) even in the region with sharp transitions.
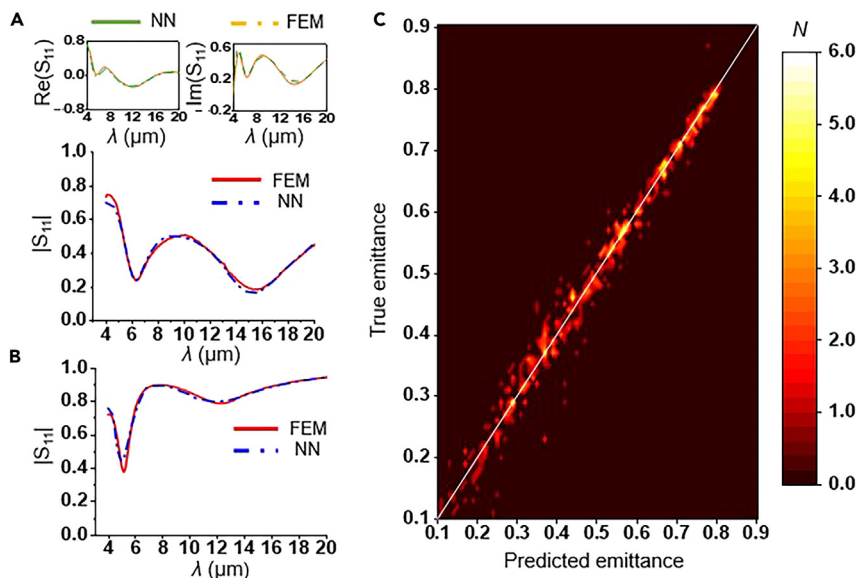
Figure 3. Evaluation of the trained neural network in forward prediction with respect to full-wave calculations
(A) Real, imaginary, and amplitude of the reflection coefficient (S_{11}) for the dynamic emitter in the metallic state.
(B) Amplitude of the reflection coefficient (S_{11}) for the dynamic emitter in the insulator state.
(C) Regression result of the true and predicted emissivity. The white line represents the regression line where the predicted emissivity coincides exactly with the true emissivity, and the color represents the corresponding sample number.

Different from the metallic-state case, the insulator-state case is associated with a generally lossless (or transparent) feature and a flat spectrum of the refractive index that changes little as the wavelength varies, which leads to corresponding flat $|S_{11}|$ spectra, especially at long wavelengths. Therefore, the insulator-state dataset might be overfitted by using the decomposition approach. However, without the presence of the spectral decomposition, as shown in Figure 3B, the predicted spectrum realizes superb agreement with the full-wave simulations with an exemplified structural parameter vector of [0.6, 0.7, 1.3, 0.1].

For the verification of generality, a dataset with 200 groups of structural parameters is examined. The regression output is given in Figure 3C, where the predicted emittance, true emittance, and occurrence probability are displayed together. The white line represents the situations where the predicted emittance exactly equals the true emittance, and the color represents the number of occurrences. As shown in Figure 3C, the vast majority of red points are clustered near the white line, which indicates the predicted emittances are highly consistent with the true emittances, manifesting excellent forward prediction accuracy and model reliability.

Optimized performance and underlying physical mechanism

The reverse design is performed to retrieve the optimal structure corresponding to the demanding performance, which is challenging because of the high degree of freedom and the large parameter space. Moreover, each design parameter might affect either the metallic-state or the insulator-state spectral responses in distinct ways. To resolve the multi-factor comprehensive optimization problem and avoid the local minimum situation, the genetic global optimization algorithm is employed with an objective function of $1 - \Delta\varepsilon = 1 - (\varepsilon_M - \varepsilon_I)$. The computational details can be referred to in Figure 1D and the STAR Methods section. Figure 4 displays the optical responses of the optimized device with a parameter vector of [1.84, 1.06, 1.55, 0.23]. As shown in Figure 4A, the $|S_{11}|$ spectra in the metallic (blue dashed line) and insulator states (black dashed line) predicted by the neural network coincide well with the full-wave finite element simulations (solid lines), suggesting excellent prediction accuracy. The corresponding emittance spectra are displayed in Figure 4B. The designed dynamic emitter shows a near-perfect emittance ($\varepsilon_M = 0.98$) at a high temperature across the whole atmospheric window (i.e., 8−13 μm); meanwhile, the emittance at the low temperature is suppressed as low as $\varepsilon_I = 0.18$. Therefore, $\Delta\varepsilon$ reaches an outstanding value of 0.8, manifesting an excellent emittance tunability that was rarely been exceeded so far (See Table S1).[16–22]
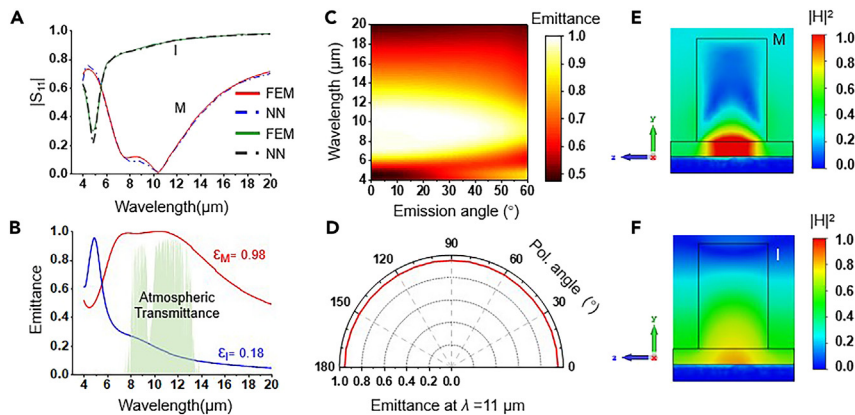
Figure 4. Optimized performance and microcosmic mechanism

(A) Direct comparison between the amplitude of the reflection coefficients obtained by neural networks and full-wave simulations.

(B) Spectral emittance of the emitter in the insulator and metallic states.

(C) Contour map of the spectral emittance as a function of incident angle.

(D) Averaged emittance as a function of the azimuthal angle at a wavelength of 11 μm.

(E and F) Magnetic field distributions of the device working in the metallic (E) and insulator states (F).

Furthermore, the angle-dependent performance of the dynamic emitter at high temperatures is explored. Figure 4C presents the contour map of emittance versus wavelength and emission angle. As shown in Figure 4C, the spectral bandwidth narrows gradually as the emission angle increases. However, the feature of near-perfect emittance within the atmospheric window still preserves at a large emission angle of 60°. To inspect the influence of polarization angles, the emittance with varying polarization angles (from 0° to 180°) is extracted while keeping the wavelength at 11 μm and the emission angle at 45°. It can be seen from Figure 4D that the emittance of the device is independent of the polarization angle, remaining constant in the vicinity of $\varepsilon = 0.98$. The feature of angular invariance further demonstrated the advantage of the optical metasurface with nanopatterned VO_2 structures.

To explore the origin of broadband near-perfect emittance, the field distributions associated with an emittance peak of 11 μm are rendered. Figures 4E and 4F display the magnetic intensity profiles for the metallic and insulator cases, respectively. As shown in Figure 4E, in a unit cell, a strong magnetic dipole is formed, because of the anti-phase electric dipole oscillations around the VO_2 meta-atoms induced by the localized surface plasmon resonance (LSPR).[45,46] Interacted with LSPR, the metallic VO_2 with a giant extinction coefficient leads to considerable nonradiative loss, which thus yields broadband emittance peaks. As the VO_2 turns into the insulator state, as shown in Figure 4F, the LSPR does not exist and the cavity mode almost disappears, bringing about low emittance values. Besides the optimization for the broadband emittance, the narrowband optimization is also feasible (see Figure S1).

Model interpretability

In addition to model accuracy, physical interpretability is also critical, which facilitates discovering the intricate relationships behind the data and then provides beneficial guidance to rational design. Figure 5A gives the feature importance with the aid of the decision tree which logically uses a series of simple tests to establish the connection between features and labels.[47,48] Compared with the black-box model (e.g., neural network), the classifier such as the decision tree has more advantages in terms of interpretability because its logical decision rules are easier to understand than the weight values of neural network nodes. As shown in Figure 5A, the features of p and l play an overwhelming role, which together account for more than 85% of the importance in the cases of $\varepsilon = 0.7$ and $\varepsilon = 0.8$. Owing to the crucial physical significance of the filling factor (i.e., $(l/p)^2$), the feature l/p instead of p is employed in the importance evaluation; otherwise, the decision tree would generate too many branches and reduce the interpretability. It can be seen from Figure 5A that, the importance of l/p continues to increase as the emittance increases, which originates from the sensitivity of LSPR to the filling factor that determines the resonance wavelength of the metasurface. In the meanwhile, the influence of t_1 gradually increases, and finally exceeds the influence of l for an emittance of 0.9, becoming the second most important feature, which indicates that, once LSPR is excited, the fine-tuning of t_1 can improve the absolute volume
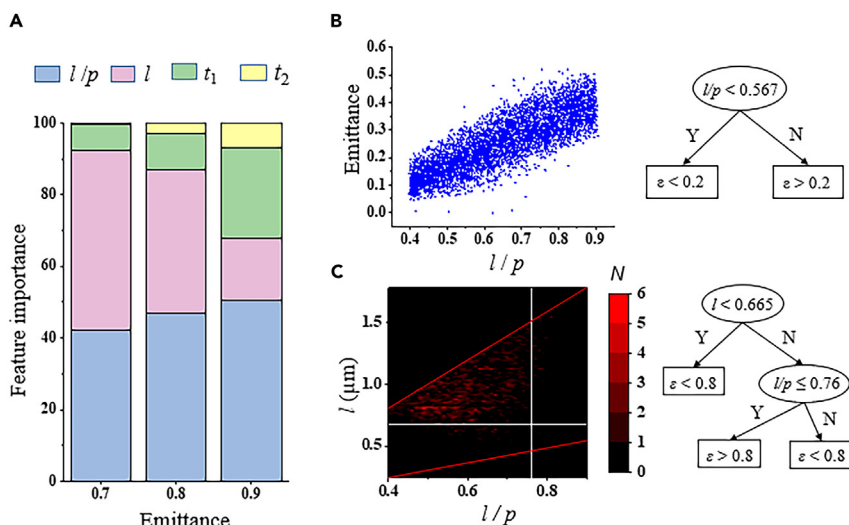
Figure 5. Inherent relations between the structural parameters and the physical quantity of emittance uncovered by the analysis of decision trees

(A) Feature importance of key parameters (l/p, l, t_1, t_2) with respect to the physical quantity of emittance.

(B) Data distribution of the low-temperature emittance at different l/p values and the corresponding decision tree.

(C) Statistical map and the underlying decision tree for the emittance of the device in the metallic state. Two red lines indicate the sampling space defined by the l and l/p. The straight white lines display the critical points and the color represents the number of samples with an emittance greater than 0.8.

of the active layer and thus the emittance. It is worth noting that all the first three important parameters, accounting for more than 90% of feature importance, are directly relevant to the VO_2 meta-atom, which indirectly suggests that the other component such as the dielectric spacer might be not that sensitive and can be substituted according to the convenience of processing.

Figure 5B presents the emittance scatterplot for the emitter in the insulator state, with the smallest decision tree. As shown in Figure 5B, the emittance is positively correlated with l/p in general, suggesting the emission in the insulator state is directly proportional to the surface coverage of VO_2. If an emittance of 0.2 is set as the design criterion, l/p should be smaller than 0.567, meaning the surface coverage of the VO_2 metasurface should be no more than 32% to fulfill the design objective of $\varepsilon < 0.2$.

The metallic state case seems a little complicated because of the extremely nonlinear light-matter interaction. According to the feature importance shown in Figure 5A, a two-level decision tree is generated with the key predictors of l and l/p. As shown in the left panel of Figure 5C, the colormap represents the occurrence of high emittance with $\varepsilon > 0.8$, the red lines show the boundary of training data and the white lines indicate the critical values that correspond to the chance nodes of $l < 0.665$ and $l/p \leq 0.76$. It can be concluded from Figure 5C that, to inversely design an emitter with high emittance (e.g., $\varepsilon > 0.8$), the VO_2 block should be not too small (i.e., $l > 0.665$), and the filling factor should be not too large (i.e., $l/p \leq 0.76$). Although these values are not necessarily exact, they can provide some physical hints and design references.

To investigate the influence of the structural parameters on the evolution trend of emittance, gradient analysis is performed. Figure 6A shows the emittance at an exemplified parameter vector of [1.62, 0.91, 1.90, 0.23] and its gradient vector with respect to each structural parameter (i.e., $\frac{\partial \varepsilon}{\partial x_i}$), where the red and blue histograms/vectors correspond to the metallic and insulator states, respectively. The magnitude of the gradient vector is proportional to the inset scale and the upward (downward) direction presents the positive (negative) sign of the gradient. It can be concluded from Figure 6A that, under present conditions, the emittance in the metallic (insulator) state can be further improved by increasing l (l, t_1, t_2) and/or decreasing p, t_1, t_2 (p), among which the measure of increasing l would exert the biggest influence because of the largest gradient magnitude.

Beyond a specific structural vector, the gradient of emittance with respect to l is further examined in a large data space. Figures 6B and 6C give $\frac{\partial \varepsilon}{\partial l}$ versus l and p for the metallic and insulator cases, respectively. As
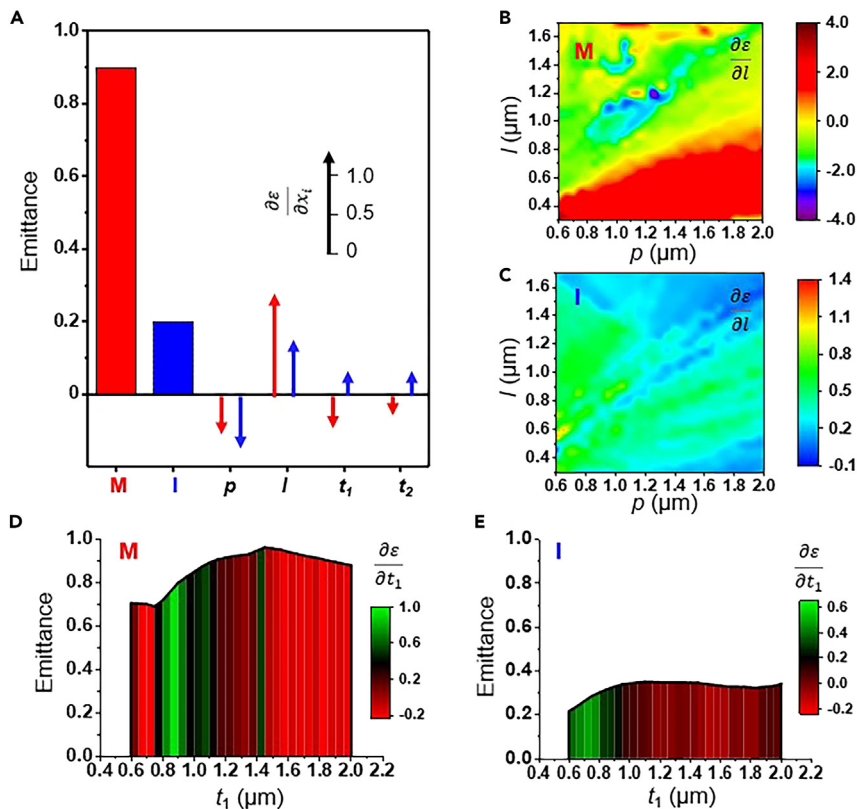
Figure 6. Gradient analysis of emittance with respect to key structural parameters

(A) Emittance at the metallic (red bar) and insulator (blue bar) states and gradient vector of emittance with respect to key parameters (p, l, t_1, t_2). The upward and downward arrows represent the positive and negative gradients respectively. The red and blue colors indicate the metallic and insulator states, respectively.

(B and C) Partial derivative of ε with respect to l for the cases of metallic state (B) and insulator state (C). Data distribution of the low-temperature emittance at different l/p values and the corresponding decision-tree structure.

(D and E) Emittance (presented by curves) as a function of t_1 and partial derivative (presented by colorbars) of ε with respect to t_1 for the cases of the metallic (D) and insulator states (E).

shown in Figure 6B, there is a rough dividing line (i.e., $\frac{\partial \varepsilon}{\partial l} = 0$) between the positive and negative gradients, which suggests the existence of the optimal l value for a certain parameter of p. For example, on the longitudinal line of p = 1.4 μm, it can be seen that $\frac{\partial \varepsilon}{\partial l}$ first increases, then reaches saturation, and finally decreases gradually as l increases from 0.3 to 1.5 μm; the optimal l tends to occur in the saturation region, or with a slight lag (e.g., 0.8 <l< 1.2 μm). Different from the metallic state case, the insulator case that requires a low emittance expects the structural parameter to be adjusted toward the negative gradients. However, as shown in Figure 6C, the positive gradient pervades almost all the (l, p) space, indicating the challenge of reducing the intrinsic emittance of the insulator case via nanostructures substantially; therefore, it becomes the next-best principle to restrain the emittance from rising too high.

According to the results obtained from the decision tree model (as shown in Figure 5), t_1 is also a nontrivial parameter to make the emittance go to extremes. To clarify the relationship between the structural gradient of t_1 and the emittance in a clearer one-dimensional perspective, Figures 6D and 6E respectively give the partial derivatives of $\frac{\partial \varepsilon}{\partial t_1}$ for the metallic and insulator cases, where the corresponding parameter vector is [1.62, 1.07, t_1, 0.12] and t_1 varies from 0.6 to 2.0 μm. It is noted that, as shown in Figure 6B, the data point of [p, l] = [1.62, 1.07] falls rightly in the saturation region with $\frac{\partial \varepsilon}{\partial l} \approx 0$. Although the l-dominated increase is saturated, the parameter t_1 might still be able to bring about a further increase. As shown in Figure 6D, with increasing t_1, the emittance slightly decreases as t_1 is small (e.g., t_1 = 0.7 μm), and then increases significantly, reaching a high emittance of 0.96 at t_1 = 1.45. In the meantime, the emittance for the insulator case (as shown in Figure 6E) is affected little by the increase of t_1 on the whole, consistent

with the conclusion from decision trees. However, as shown in Figure 6E, the emittance is even slightly decreased with a negative gradient in the vicinity of t_1 = 1.5, which facilitates enhancing the emittance tunability and falls exactly in line with the design expectations.

DISCUSSION

Aiming at the potential application of dynamic radiative cooling, we have studied the VO_2-based metasurface with a metal-insulator-metal architecture, with the aid of an ensemble of data-driven methods. The neural network is constructed and well-trained to predict the optical response of the dynamic emitter with remarkable accuracy comparable to full-wave simulations, which is then coupled to the genetic algorithm for inverse design. To improve the accuracy and computational speed, spectral decomposition and transfer learning strategies are employed, which adapt the neural network to be qualified successfully to the concerned problem of dynamic emitters. Compared to conventional case-by-case design, the combination of machine learning and the dynamic emitter bring about many advantages. First, despite the structural simplicity, the metasurface has been optimized with an outstanding emittance and an emittance tunability that have rarely been exceeded so far. The fundamental reason is that the data-driven optimization can search the optimal parameters from the *continuous* dataspace ensured by the well-trained neural network model which is far beyond the *discrete* dataspace generated by the parameter-scanning simulation. Besides the interpolation-like feature of the well-trained neural network, the extrapolating function outside but close to the training scope is also theoretically feasible. Second, the accelerated speed of the neural network enables thousands of iterations possible for the time-consuming three-dimensional full-wave optimization. Finally, machine-learning toolkits such as the decision tree and gradient analysis can not only uncover the latent relationship between the structure and optical response semi-quantitatively but also shed more light on the underlying physics qualitatively. Though the investigation has focused on dynamic emitters, the combined data-driven approach can also provide opportunities for other thermal and photonic devices with versatile functionality.

Limitations of study

Taking account into the convenience of scalable fabrication, the investigated phase-change metasurface is confined to a regular geometric topology. However, with the rapid development of nanotechnology, more and more metasurfaces with complex meta-atom and topologic configurations can be prepared with high quality and cost-effectively. Therefore, from a theoretical perspective, the topology optimization of the phase-change meta-atom is still interesting work that might provide new opportunities to improve the performance and hence deserve to be done further in the field of dynamic radiative coolers. Second, as for a dynamic device, the VO_2-based thermal emitter undergoes a time-dependent phase-transition process and has transient intermediate states between the initial and final steady states; however, the transient intermediate states are not considered in the manuscript for simplification. Moreover, not limited to VO_2, other phase-change materials such as Ge-Sb-Te (GST) and Ge-Sb-Se-Te (GSST) can also be considered as another degree of freedom in the design[49–51] and the experimental realization is desired in the future.

STAR★METHODS

Detailed methods are provided in the online version of this paper and include the following:

- KEY RESOURCES TABLE
- RESOURCE AVAILABILITY
  - Lead contact
  - Materials availability
  - Data and code availability
- EXPERIMENTAL MODEL AND SUBJECT DETAILS
- METHOD DETAILS
  - Data generation and preprocessing
- NEURAL NETWORK TRAINING
  - Decision tree and genetic algorithm models
- QUANTIFICATION AND STATISTICAL ANALYSIS
- ADDITIONAL RESOURCES

SUPPLEMENTAL INFORMATION

Supplemental information can be found online at https://doi.org/10.1016/j.isci.2023.106857.

REFERENCES

1. Wang, S., Jiang, T., Meng, Y., Yang, R., Tan, G., and Long, Y. (2021). Scalable thermochromic smart windows with passive radiative cooling regulation. Science *374*, 1501–1504. https://doi.org/10.1126/science.abg0291.

2. Tang, K., Dong, K., Li, J., Gordon, M.P., Reichertz, F.G., Kim, H., Rho, Y., Wang, Q., Lin, C.-Y., Grigoropoulos, C.P., et al. (2021). Temperature-adaptive radiative coating for all-season household thermal regulation. Science *374*, 1504–1509. https://doi.org/10.1126/science.abf7136.

3. Xu, X., Gu, J., Zhao, H., Zhang, X., Dou, S., Li, Y., Zhao, J., Zhan, Y., and Li, X. (2022). Passive and dynamic phase-change-based radiative cooling in outdoor weather. ACS Appl. Mater. Interfaces *14*, 14313–14320. https://doi.org/10.1021/acsami.1c23401.

4. Xi, W., Liu, Y., Zhao, W., Hu, R., and Luo, X. (2021). Colored radiative cooling: how to balance color display and radiative cooling performance. Int. J. Therm. Sci. *170*, 107172. https://doi.org/10.1016/j.ijthermalsci.2021.107172.

5. Zhu, H., Li, Q., Tao, C., Hong, Y., Xu, Z., Shen, W., Kaur, S., Ghosh, P., and Qiu, M. (2021). Multispectral camouflage for infrared, visible, lasers and microwave with radiative cooling. Nat. Commun. *12*, 1805. https://doi.org/10.1038/s41467-021-22051-0.

6. Zhu, H., Li, Q., Zheng, C., Hong, Y., Xu, Z., Wang, H., Shen, W., Kaur, S., Ghosh, P., and Qiu, M. (2020). High-temperature infrared camouflage with efficient thermal management. Light Sci. Appl. *9*, 60. https://doi.org/10.1038/s41377-020-0300-5.

7. Liu, Y., Zuo, H., Xi, W., Hu, R., and Luo, X. (2022). Flexible janus functional film for adaptive thermal camouflage. Adv. Mater. Technol. *7*, 2100821. https://doi.org/10.1002/admt.202100821.

8. Liu, Y., Song, J., Zhao, W., Ren, X., Cheng, Q., Luo, X., Fang, N.X., and Hu, R. (2020). Dynamic thermal camouflage via a liquid-crystal-based radiative metasurface. Nanophotonics *9*, 855–863. https://doi.org/10.1515/nanoph-2019-0485.

9. Hu, R., Xi, W., Liu, Y., Tang, K., Song, J., Luo, X., Wu, J., and Qiu, C.-W. (2021). Thermal camouflaging metamaterials. Mater. Today *45*, 120–141. https://doi.org/10.1016/j.mattod.2020.11.013.

10. Kort-Kamp, W.J.M., Kramadhati, S., Azad, A.K., Reiten, M.T., and Dalvit, D.A.R. (2018). Passive radiative "Thermostat" enabled by phase-change photonic nanostructures. ACS Photonics *5*, 4554–4560. https://doi.org/10.1021/acsphotonics.8b01026.

11. Zhao, H., Zhan, Y., Dou, S., Wang, L., Li, Y., and Li, X. (2021). Passive radiative temperature regulator: principles and absorption-emission manipulation. Sol. Energy Mater. Sol. Cells *229*, 111143. https://doi.org/10.1016/j.solmat.2021.111143.

12. Lin, C., Hur, J., Chao, C.Y.H., Liu, G., Yao, S., Li, W., and Huang, B. (2022). All-weather thermochromic windows for synchronous solar and thermal radiation regulation. Sci. Adv. *8*, eabn7359. https://doi.org/10.1126/sciadv.abn7359.

13. Cui, Y., Ke, Y., Liu, C., Chen, Z., Wang, N., Zhang, L., Zhou, Y., Wang, S., Gao, Y., and Long, Y. (2018). Thermochromic VO$_2$ for energy-efficient smart windows. Joule *2*, 1707–1746. https://doi.org/10.1016/j.joule.2018.06.018.

14. Dou, S., Zhao, J., Zhang, W., Zhao, H., Ren, F., Zhang, L., Chen, X., Zhan, Y., and Li, Y. (2020). A universal approach to achieve high luminous transmittance and solar modulating ability simultaneously for vanadium dioxide smart coatings via double-sided localized surface plasmon resonances. ACS Appl. Mater. Interfaces *12*, 7302–7309. https://doi.org/10.1021/acsami.9b17923.

15. Dong, K., Tseng, D., Li, J., Warkander, S., Yao, J., and Wu, J. (2022). Reducing temperature swing of space objects with temperature-adaptive solar or radiative coating. Cell Rep. Phys. Sci. *3*, 101066. https://doi.org/10.1016/j.xcrp.2022.101066.

16. Taylor, S., Boman, N., Chao, J., and Wang, L. (2021). Cryothermal vacuum measurement of thermochromic variable-emittance coatings with heating/cooling hysteresis for spacecraft thermal management. Appl. Therm. Eng. *199*, 117561. https://doi.org/10.1016/j.applthermaleng.2021.117561.

17. Yang, F., Hu, X., Fei, Y., Kim, S.-K., Luo, X., and Hu, R. (2022). Near-field thermophotonic system for power generation and electroluminescent refrigeration. Rev. Sci. Instrum. *93*, 053902. https://doi.org/10.1063/5.0076765.

18. Xi, W., Liu, Y., Song, J., Hu, R., and Luo, X. (2021). High-throughput screening of a high-Q mid-infrared Tamm emitter by material informatics. Opt. Lett. *46*, 888–891. https://doi.org/10.1364/OL.417378.

19. Hu, R., Song, J., Liu, Y., Xi, W., Zhao, Y., Yu, X., Cheng, Q., Tao, G., and Luo, X. (2020). Machine learning-optimized Tamm emitter for high-performance thermophotovoltaic system with detailed balance analysis. Nano Energy *72*, 104687. https://doi.org/10.1016/j.nanoen.2020.104687.

20. Morin, F.J. (1959). Oxides which show a metal-to-insulator transition at the neel temperature. Phys. Rev. Lett. *3*, 34–36. https://doi.org/10.1103/PhysRevLett.3.34.

21. Ke, Y., Chen, J., Lin, G., Wang, S., Zhou, Y., Yin, J., Lee, P.S., and Long, Y. (2019). Smart windows: electro-thermo-mechano-photochromics, and beyond. Adv. Energy

Mater. *9*, 1902066. https://doi.org/10.1002/aenm.201902066.

22. Ulpiani, G., Ranzi, G., Shah, K.W., Feng, J., and Santamouris, M. (2020). On the energy modulation of daytime radiative coolers: a review on infrared emissivity dynamic switch against overcooling. Sol. Energy *209*, 278–301. https://doi.org/10.1016/j.solener.2020.08.077.

23. Taylor, S., Yang, Y., and Wang, L. (2017). Vanadium dioxide based Fabry-Perot emitter for dynamic radiative cooling applications. J. Quant. Spectrosc. Radiat. Transf. *197*, 76–83. https://doi.org/10.1016/j.jqsrt.2017.01.014.

24. Taylor, S., Long, L., McBurney, R., Sabbaghi, P., Chao, J., and Wang, L. (2020). Spectrally-selective vanadium dioxide based tunable metafilm emitter for dynamic radiative cooling. Sol. Energy Mater. Sol. Cells *217*, 110739. https://doi.org/10.1016/j.solmat.2020.110739.

25. Omam, Z.R., Ghobadi, A., Khalichi, B., and Ozbay, E. (2022). Fano resonance in a dolomite phase-change multilayer design for dynamically tunable omnidirectional monochromatic thermal emission. Opt. Lett. *47*, 5781–5784. https://doi.org/10.1364/OL.475253.

26. Xing, G., Zhao, W., Hu, R., and Luo, X. (2021). Spatiotemporal modulation of thermal emission from thermal-hysteresis vanadium dioxide for multiplexing thermotronics functionalities. Chinese Phys. Lett. *38*, 124401. https://doi.org/10.1088/0256-307X/38/12/124401.

27. Shrewsbury, B.K., Morsy, A.M., and Povinelli, M.L. (2022). Multilayer planar structure for optimized passive thermal homeostasis [Invited]. Opt. Mater. Express *12*, 1442–1449. https://doi.org/10.1364/OME.435519.

28. Sun, K., Riedel, C.A., Urbani, A., Simeoni, M., Mengali, S., Zalkovskij, M., Bilenberg, B., de Groot, C.H., and Muskens, O.L. (2018). VO$_2$ thermochromic metamaterial-based smart optical solar reflector. ACS Photonics *5*, 2280–2286. https://doi.org/10.1021/acsphotonics.8b00119.

29. Ono, M., Chen, K., Li, W., and Fan, S. (2018). Self-adaptive radiative cooling based on phase change materials. Opt Express *26*, A777–A787. https://doi.org/10.1364/OE.26.00A777.

30. Buhara, E., Ghobadi, A., Khalichi, B., Kocer, H., and Ozbay, E. (2021). Mid-infrared adaptive thermal camouflage using a phase-change material coupled dielectric nanoantenna. J. Phys. D Appl. Phys. *54*, 265105. https://doi.org/10.1088/1361-6463/abf53d.

31. Long, L., Taylor, S., and Wang, L. (2020). Enhanced infrared emission by thermally switching the excitation of magnetic polariton with scalable microstructured VO$_2$ metasurfaces. ACS Photonics *7*, 2219–2227. https://doi.org/10.1021/acsphotonics.0c00760.

32. Jia, Y., Wang, X., Yin, H., Yao, H., Wang, J., and Fan, C. (2021). Highly tunable thermal emitter with vanadium dioxide metamaterials for radiative cooling. Appl. Opt. *60*, 5699–5706. https://doi.org/10.1364/AO.421977.

33. Zhang, W.-W., Qi, H., Sun, A.-T., Ren, Y.-T., and Shi, J.-W. (2020). Periodic trapezoidal VO$_2$-Ge multilayer absorber for dynamic radiative cooling. Opt Express *28*, 20609–20623. https://doi.org/10.1364/OE.396171.

34. Lei, L., Lou, F., Tao, K., Huang, H., Cheng, X., and Xu, P. (2019). Tunable and scalable broadband metamaterial absorber involving VO$_2$-based phase transition. Photon. Res. *7*, 734–741. https://doi.org/10.1364/PRJ.7.000734.

35. Li, W., Chen, P., Xiong, B., Liu, G., Dou, S., Zhan, Y., Zhu, Z., Chu, T., Li, Y., and Ma, W. (2022). Deep learning modeling strategy for material science: from natural materials to metamaterials. J. Phys. Mater. *5*, 014003. https://doi.org/10.1088/2515-7639/ac5914.

36. Xu, Y., Zhang, X., Fu, Y., and Liu, Y. (2021). Interfacing photonics with artificial intelligence: an innovative design strategy for photonic structures and devices based on artificial neural networks. Photon. Res. *9*, B135–B152. https://doi.org/10.1364/PRJ.417693.

37. Ma, W., Liu, Z., Kudyshev, Z.A., Boltasseva, A., Cai, W., and Liu, Y. (2021). Deep learning for the design of photonic structures. Nat. Photonics *15*, 77–90. https://doi.org/10.1038/s41566-020-0685-y.

38. Ma, W., Cheng, F., Xu, Y., Wen, Q., and Liu, Y. (2019). Probabilistic representation and inverse design of metamaterials based on a deep generative model with semi-supervised learning strategy. Adv. Mater. *31*, 1901111. https://doi.org/10.1002/adma.201901111.

39. Ma, W., Cheng, F., and Liu, Y. (2018). Deep-learning-enabled on-demand design of chiral metamaterials. ACS Nano *12*, 6326–6334. https://doi.org/10.1021/acsnano.8b03569.

40. Panda, S.S., Choudhary, S., Joshi, S., Sharma, S.K., and Hegde, R.S. (2022). Deep learning approach for inverse design of metasurfaces with a wider shape gamut. Opt. Lett. *47*, 2586–2589. https://doi.org/10.1364/OL.458746.

41. Lininger, A., Hinczewski, M., and Strangi, G. (2021). General inverse design of layered thin-film materials with convolutional neural networks. ACS Photonics *8*, 3641–3650. https://doi.org/10.1021/acsphotonics.1c01498.

42. Nadell, C.C., Huang, B., Malof, J.M., and Padilla, W.J. (2019). Deep learning for accelerated all-dielectric metasurface design. Opt Express *27*, 27523–27535. https://doi.org/10.1364/OE.27.027523.

43. Sheverdin, A., Monticone, F., and Valagiannopoulos, C. (2020). Photonic inverse design with neural networks: the case of invisibility in the visible. Phys. Rev. Appl. *14*, 024054. https://doi.org/10.1103/PhysRevApplied.14.024054.

44. Luo, J., Li, X., Zhang, X., Guo, J., Liu, W., Lai, Y., Zhan, Y., and Huang, M. (2021). Deep-learning-enabled inverse engineering of multi-wavelength invisibility-to-superscattering switching with phase-change materials. Opt Express *29*, 10527–10537. https://doi.org/10.1364/OE.422119.

45. Sun, S., He, Q., Hao, J., Xiao, S., and Zhou, L. (2019). Electromagnetic metasurfaces: physics and applications. Adv. Opt Photon *11*, 380–479. https://doi.org/10.1364/AOP.11.000380.

46. Zhan, Y., Zhang, L., Rahmani, M., Giannini, V., Miroshnichenko, A.E., Hong, M., Li, X., Maier, S.A., and Lei, D. (2021). Synthetic plasmonic nanocircuits and the evolution of their correlated spatial arrangement and resonance spectrum. ACS Photonics *8*, 166–174. https://doi.org/10.1021/acsphotonics.0c01756.

47. Kotsiantis, S.B. (2013). Decision trees: a recent overview. Artif. Intell. Rev. *39*, 261–283. https://doi.org/10.1007/s10462-011-9272-4.

48. Elzouka, M., Yang, C., Albert, A., Prasher, R.S., and Lubner, S.D. (2020). Interpretable forward and inverse design of particle spectral emissivity using common machine-learning models. Cell Rep. Phys. Sci. *1*, 100259. https://doi.org/10.1016/j.xcrp.2020.100259.

49. Liu, K., Li, Y., Qin, K., and Cao, T. (2020). Tuning of classical electromagnetically induced reflectance in babinet chalcogenide metamaterials. iScience *23*, 101367. https://doi.org/10.1016/j.isci.2020.101367.

50. Zhang, S., Chen, X., Liu, K., Li, H., Lang, Y., Han, J., Wang, Q., Lu, Y., Dai, J., Cao, T., et al. (2022). Terahertz multi-level nonvolatile optically rewritable encryption memory based on chalcogenide phase-change materials. iScience *25*, 104866. https://doi.org/10.1016/j.isci.2022.104866.

51. Ko, J.H., Kim, D.H., Hong, S.-H., Kim, S.-K., and Song, Y.M. (2023). Polarization-driven thermal emission regulator based on self-aligned GST nanocolumns. iScience *26*, 105780. https://doi.org/10.1016/j.isci.2022.105780.

52. Morsy, A.M., Barako, M.T., Jankovic, V., Wheeler, V.D., Knight, M.W., Papadakis, G.T., Sweatlock, L.A., Hon, P.W.C., and Povinelli, M.L. (2020). Experimental demonstration of dynamic thermal regulation using vanadium dioxide thin films. Sci. Rep. *10*, 13964. https://doi.org/10.1038/s41598-020-70931-0.

53. Xinyuan, Z., Wang, J., Li, Y., Yang, R., and Zhan, Y. (2022). Spectral decoupling of cooperative emissivity in silica-polymer metamaterials for radiative cooling. Opt. Lett. *47*, 2506–2509. https://doi.org/10.1364/OL.455302.

54. Wang, J., Tan, G., Yang, R., and Zhao, D. (2022). Materials, structures, and devices for dynamic radiative cooling. Cell Rep. Phys. Sci. *3*, 101198. https://doi.org/10.1016/j.xcrp.2022.101198.

55. Ma, H., Yao, K., Dou, S., Xiao, M., Dai, M., Wang, L., Zhao, H., Zhao, J., Li, Y., and Zhan, Y. (2020). Multilayered SiO$_2$/Si$_3$N$_4$ photonic emitter to achieve high-performance all-day radiative cooling. Sol. Energy Mater. Sol. Cells *212*, 110584. https://doi.org/10.1016/j.solmat.2020.110584.

STAR★METHODS

KEY RESOURCES TABLE

REAGENT or RESOURCE	SOURCE	IDENTIFIER
Deposited data		
Figshare repository with data	This paper	https://doi.org/10.6084/m9.figshare.22730780
Figshare repository with codes	This paper	https://doi.org/10.6084/m9.figshare.22730864
Software and algorithms		
Python 3.6	Python Software Foundation	https://www.python.org/
Pycharm 2021	JetBrains	https://www.jetbrains.com/pycharm/
Tensorflow 2.3.0	GitHub	https://github.com/tensorflow/tensorflow
Sklearn0.23.2	Google	http://scikit-learn.org/

RESOURCE AVAILABILITY

Lead contact

Further information and other requests should be directed to and will be fulfilled by the lead contact, Xiao-feng LI (xfli@suda.eud.cn).

Materials availability

This work did not generate new unique reagents.

Data and code availability

- Structural and spectral data have been deposited at Figshare and are publicly available as of the date of publication. DOIs are listed in the key resources table.

- All original code has been deposited at Figshare and is publicly available as of the date of publication. DOIs are listed in the key resources table.

- Any additional information required to reanalyze the data reported in this paper is available from the lead contact upon request.

EXPERIMENTAL MODEL AND SUBJECT DETAILS

This work is relevant to the light-matter interaction in the optical nanostructures, and did not use any biological models or any animal/human subjects/samples. The specific modeling details can be referred to as method details.

METHOD DETAILS

Data generation and preprocessing

The numerical range of the structural parameters is predefined as $P \in [0.6, 2.0]$, $l \in [0.4 P, 0.9P]$, $t_1 \in [0.6, 2.0]$, $t_2 \in [0.1, 0.4]$ (in units of μm). It is about 5000 groups of structural parameters that are randomly generated, and their spectral responses at both metallic and insulator states are calculated by using the full-wave method, which is performed using the finite element solver in conjunction with Python. The refractive index of VO_2 is obtained from the experimental measurement.[52] The spectral range is considered from 4 to 20 μm and 169 wavelength points are sampled corresponding to the 169 outputs of the neural networks. According to the reciprocity principle of thermal radiation, the spectral emittance is calculated as follows,

$$\varepsilon(\lambda, T) = A(\lambda, T) = 1 - |S_{11}(\lambda, T)|^2 \qquad \text{(Equation 2)}$$

Where ε is the emittance, A the absorbance, S_{11} the reflection coefficient. The integrated emittance is calculated as the ratio of the emissive power of the metasurface to the transmitted power of the blackbody at the same temperature in the atmospheric window band ($8 - 13\ \mu m$) where thermal emission can escape successfully to the deep space,[2,53–55]

$$\varepsilon(\lambda, T) = \frac{\int_{8\mu m}^{13\mu m} I_{bb}(\lambda, T)\varepsilon(\lambda, T)\mathrm{d}\lambda}{\int_{8\mu m}^{13\mu m} I_{bb}(\lambda, T)\mathrm{d}\lambda} \qquad \text{(Equation 3)}$$

where $I_{bb}(\lambda, T)$ represents the spectral intensity of the standard blackbody emission at temperature T, and $\varepsilon(\lambda, T)$ represents the spectral emittance of the sample.

NEURAL NETWORK TRAINING

The neural network uses mean square error (MSE) as a loss function to monitor the updating of parameter θ. MSE is defined as,

$$MSE = \frac{1}{N}\sum_{i=1}^{N}(y_i - \widehat{y}_i)^2 \qquad \text{(Equation 4)}$$

where N is the sample size, y_i the predicted value, $\widehat{y}_i$ the true value. The neural network used to predict the real part response of the structure used a total of 5000 sets of data (80% for training and 20% for testing). After 2000 iterations of training, the overall test error of the real part training network reaches 2.5×10^{-3}. We choose *tanh* and *sigmoid* as the activation function in the neural networks for the metallic and insulator cases, respectively. The learning rate of 0.01 and the Adam optimizer are chosen in both cases. All training is performed using TensorFlow 2.3.0 on NVIDIA GeForce GTX 1650 SUPER graphics card.

Decision tree and genetic algorithm models

In the decision tree model, the emittance is set as the output variable and the structural parameters are set as predictors. The smallest tree pruning is used to avoid over-fitting and an excessive number of decision nodes. The maximum depth is set as 2 and 1 for the metallic and insulator cases; the minimum sample sizes of the branch and the leaf node are both set at 30. The labels were divided into two categories using the thresholds of 0.8 and 0.2 for the metallic and insulator cases. The scikit-opt framework is employed for the genetic algorithm and the script details can be referred to in the key resources table.

QUANTIFICATION AND STATISTICAL ANALYSIS

Electromagnetic simulations were performed using COMSOL Multiphysics. Figures were produced with Python from the raw data.

ADDITIONAL RESOURCES

Any additional information about the simulation and data reported in this paper is available from the lead contact on request.